Results in Physics 16 (2020) 102936

Contents lists available at ScienceDirect

Results in Physics

journal homepage: www.elsevier.com/locate/rinp

Experimental and theoretical investigation of localized CO_2 laser interaction with fused silica during the process of surface damage mitigation

Chao Tan[a], Linjie Zhao[a], Mingjun Chen[a,*], Jian Cheng[a,*], Chunya Wu[a], Qi Liu[a], Hao Yang[a], Zhaoyang Yin[a], Wei Liao[b]

[a] State Key Laboratory of Robotics and System, Harbin Institute of Technology, Harbin 150001, China
[b] Research Center of Laser Fusion, China Academy of Engineering Physics, Mianyang 621900, China

ARTICLE INFO

Keywords:
Fused silica
Damage mitigation
CO_2 laser
Surface topography evolution
Physical mechanism

ABSTRACT

Localized CO_2 laser repairing of surface damage on fused silica optics has been successfully applied in high-power laser system in the field of controllable nuclear fusion. In order to accurately predict the surface topography evolution and to reveal the intrinsic physical mechanism during the process of laser mitigation, experiments of localized CO_2 laser mitigation were firstly carried out to analyze the features of mitigated craters under different laser powers. Then a multi-physics coupled mathematical model was developed based on the fluid control equation, heat and mass transfer equation and material phase transition kinetics to investigate the thermodynamic and kinetic behaviors of laser interaction with silica. The model considered the effects of Marangoni convection, gravity, capillary force and vaporization recoil pressure, as well as the nonlinear variation of physical parameters of silica material with respect to temperature. The results showed that with the increase of laser power, the material ablation and the appearance of raised rim occurred simultaneously. The depth of the mitigated crater increased sharply when the threshold for material ablation was attained, while the lateral dimension increased linearly. The vaporization recoil pressure was found to be the dominant factor for the formation of Gaussian crater with the raised rim feature. The capillary force caused the material at the edge of the molten pool to have a tendency to reflow after laser shutting down, but it was too small to change the surface topography. This work could significantly contribute to the understanding of laser mitigation process, which laid the foundation for the accurate prediction and evaluation of surface quality of CO_2 laser repaired fused silica surface.

Introduction

In view of the high absorption rate of fused silica to CO_2 lasers with specific wavelength, as well as the improvement of laser power, CO_2 laser is used to locally melt or even evaporate the material to form a functional specific structure or morphology on the surface of fused silica components. This type of processing has been widely used in scientific research and industrial production, such as precision machining of optical components [1], processing of optical fibers [2], fabrication of optical micro-lens array and holographic structure [3,4], polishing of optical component surface [5]. In recent years, localized CO_2 laser repairing of micro-defects on the surface of fused silica optics applied in high-power laser devices is getting more and more attention, such as surface damage mitigation [6–9] and repairing of surface scratches [10,11]. It has been widely accepted that CO_2 laser repairing can greatly inhibit the growth of surface damage with small mitigation area and excellent light transmission. This CO_2 laser repairing method can effectively improve the laser damage resistance of fused silica optics as well [12,13], which has been successfully applied in high-power laser systems in the field of controllable nuclear fusion, such as USA National Ignition Facility [14], France Laser Mega-Joule [15], China huge laser facility [16].

In the process of practical localized CO_2 laser repairing of surface damage, small damage pits on the surface of fused silica optics can be irradiated continuously by CO_2 laser with a wavelength of 10.6 μm to melt the material and heal the cracks at the bottom of pits, forming a smooth Gaussian crater to achieve the purpose of laser damage growth mitigation [17,18]. However, a raised rim structure will be formed around the mitigated pit in the actual repairing process, and this morphological feature may induce a strong optical modulation to the laser propagation, which is harmful to operation of downstream optics [19]. Moreover, if not treated in time, the deposited debris on the

* Corresponding authors at: P.O. Box 413, Harbin 150001, China.
E-mail addresses: chenmj@hit.edu.cn (M. Chen), cheng.826@hit.edu.cn (J. Cheng).

https://doi.org/10.1016/j.rinp.2020.102936
Received 3 December 2019; Received in revised form 8 January 2020; Accepted 8 January 2020
Available online 10 January 2020

surface due to the evaporation of material will induce new damage under subsequent laser irradiation [20–22]. Therefore, the surface topography and surface quality of the mitigation region are important indicators for evaluating the mitigation effect of the fused silica optics, which is an urgent challenge to be solved.

Many researchers had performed a substantial amount of experiments on CO_2 laser melting mitigation, mainly focusing on the analysis of the influence of repairing parameters on surface topography features, performance evaluation of mitigation area and establishment of repairing strategy [7,23–25]. Dai et al. [17] measured the evolution of craters under different laser beam diameters, irradiation times and laser powers. Robin et al. [26] used infrared camera to measure the surface temperature of fused silica under different laser power, and established a theoretical model for the calculation of the depth of mitigation pit. Jiang et al. [27] analyzed the evolution of the mitigated crater during the CO_2 laser mitigation process and the influence of the heat affected zone on laser propagation and chemical etching rate. On the other hand, some researchers used numerical simulation to study the thermodynamic and kinetic behaviors of fused silica irradiated by CO_2 laser, such as heating and melting, material flowing, evaporation ablation [28]. Feit et al. [29] firstly established theoretical models for heating, evaporation, material flowing, crack healing during CO_2 laser mitigation, and studied the influence of nonlinear heat transfer on temperature distribution of fused silica. It was found that the effect of recoil force, melt flow and crack healing would affect the final surface quality. Yang et al. [8] compared the mitigation effect with laser wavelengths of 4.6 μm and 10.6 μm, and obtained the fictive temperature distribution and the size of the heat affected zone. It was concluded that CO_2 laser with a wavelength of 4.6 μm had a better mitigation effect on surface damage with deeper cracks. Doualle et al. [30,31] carried out 2D and 3D thermo-mechanical simulations of CO_2 laser interaction with fused silica, and obtained the temperature distribution, material ejection and residual stress distribution, these results were consistent with the analysis obtained by infrared temperature measurement, profilometry, and photo-elastic measurement. He et al. [5] studied the intrinsic physical mechanism of laser polishing fused silica surface by establishing a multi-physics transient model coupled with heat transfer and fluid flow, and analyzed the effects of surface tension, Marangoni effect, light pressure and gravity on surface smoothing. It was found that surface tension played a decisive role in polishing quality.

The above studies show that CO_2 laser interaction with fused silica is a complex multi-physics coupling process. The material chronologically undergoes different stages of heating, softening, viscous flow, evaporation ablation, and cooling freezing. It involves the heat transfer of phase change and the nonlinear variation of physical properties of silica material. At different stages, there are many intrinsic factors that influence the evolution of the surface topography, such as Marangoni effect, gravity, capillary force, and vaporization recoil pressure, and all of which change with the laser action time. The current studies focus on the optimization of processing parameters of CO_2 laser mitigation and the evaluation of mitigation effects. On the other hand, the theoretical research mainly focuses on the derivation of mathematical models, the thermodynamic calculations of laser irradiating fused silica, and the dynamic analysis of laser polishing fused silica. There are few calculations for thermodynamics and kinetics behaviors of fused silica during the process of laser mitigation. All of previous models ignored the effect of vaporization recoil pressure on mitigated crater formation, however which always appears along with material ablation. It can be concluded that the surface topography evolution of the mitigated crater on the surface of the fused silica optics have been not systematically studied, as well as the intrinsic physical mechanism of crater formation is still unclear, which are huge obstacles for the improvements of mitigation effect and batch stability of CO_2 laser repaired fused silica surfaces. Additionally, the influence law between various intrinsic factors (e.g., Marangoni effect, capillary force, and vaporization recoil pressure) urgently need to be further clarified.

In this work, the morphology features of mitigated pits were firstly analyzed through CO_2 laser mitigation experiments, and the mapping relationship between processing parameters and size of mitigated craters was investigated. To further study the process of surface topography evolution and reveal the formation mechanism of mitigated craters, a multi-physics coupled mathematical model was developed based on the fluid control equation, heat and mass transfer equation and material phase transition kinetics to investigate the thermodynamic and kinetic behaviors of laser interaction with silica. The model considered the effects of Marangoni effect, gravity, capillary force and vaporization recoil pressure, as well as the nonlinear variation of material physical parameters with respect to temperature. The influence law between various intrinsic factors during different stages of laser interaction with fused silica was studied. This work could significantly contribute to the understanding of laser mitigation process, which laid the foundation for the accurate prediction and evaluation of surface quality of CO_2 laser repaired fused silica surface.

Experiments of localized CO_2 laser mitigation

Experimental method

The samples used in the experiments were made of Corning 7980 fused silica glasses and polished to make the surface quality meet requirements, all of which were in the shape of cuboid with length of 50 mm, width of 50 mm and thickness of 5 mm. The damage pits were fabricated on the surface of fused silica samples irradiated by ultraviolet laser with wavelength of 355 nm, pulse width of 8 ns, focal spot area of 3 mm^2 and laser intensity of 20 J/cm^2. The surface topographies of pits were observed by Nikon ECLIPSE E600 optical microscope and

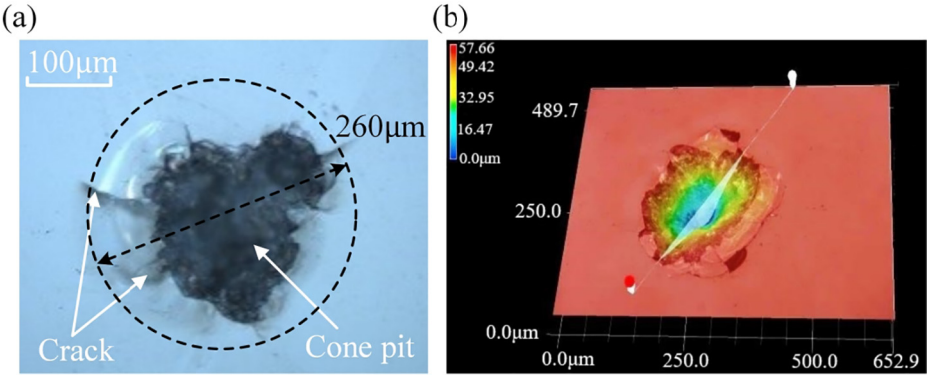

Fig. 1. Original laser damage site on fused silica surface. (a) Morphology observation measured by optical microscope; (b) Three-dimensional appearance measured by optical profiler.

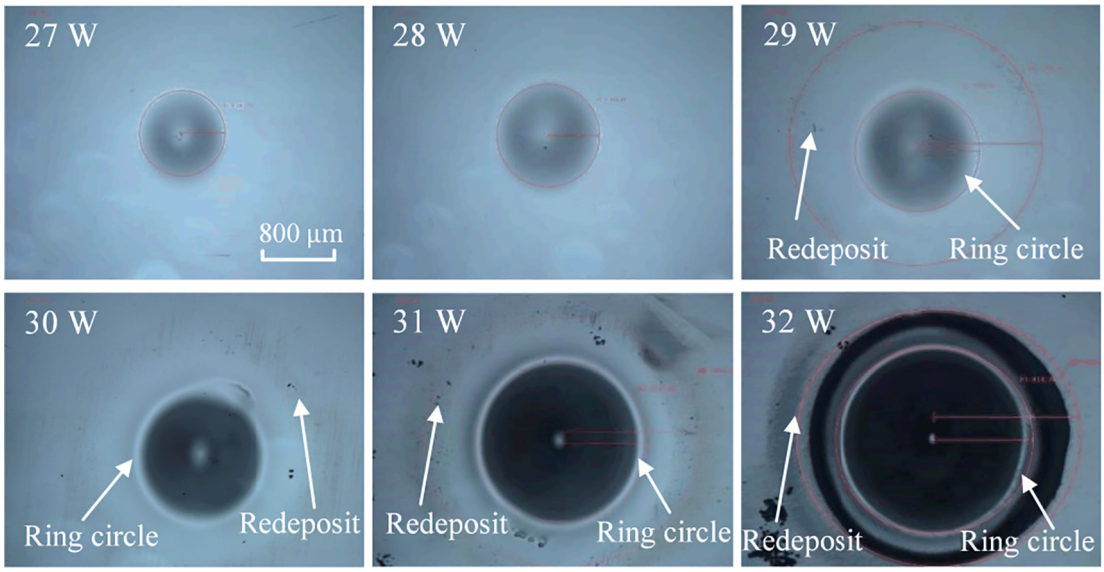

Fig. 2. The microscope micrographs of mitigated pits under different laser powers measured by optical microscope.

optical profiler, one of which is shown in Fig. 1. This kind of damage pit belongs to the "violet" type, with the lateral dimension of about 260 μm, and the longitudinal depth of about 60 μm.

The laser used in surface damage mitigation experiments was CW CO_2 laser with wavelength of 10.6 μm, spatial Gaussian distribution, and spot diameter of about 2 mm at $1/e^2$. The laser powers were set to be 27 W, 28 W, 29 W, 30 W, 31 W, 32 W in turn, and the irradiation time at each power was 5 s. Bright-field detection system was used to on-line monitor the status of damage sites during the repairing process. Taylor Hobson profiler was used to measure the two-dimensional morphology of mitigated pits.

Experimental results and analysis

The microscope observations of the mitigated pits obtained by CO_2 laser processing with different laser powers are shown in Fig. 2. It can be clearly observed that the sizes of the mitigated pits increase with the laser power. Some redeposited debris appear around the crater at the power of 29 W, which indicates that material evaporation ablation occurs during the mitigation process. Fig. 2 shows that the higher the power is, the more severe the ablation is, and the worse the mitigation effect gets.

Fig. 3 exhibits the profiles of the mitigated pits shown in Fig. 2. It can be seen that an obvious raised rim and a bright annular ring appear around the mitigated pit when the laser power increases to 29 W, which is the laser power at which material ablation occurs. With the increase of laser power, the raised rim becomes higher and higher, and the annular ring gets brighter and brighter. It can be concluded that the material ablation and the formation of raised rim occur simultaneously during the laser mitigation process. Additionally, the more severe the material ablation is, the more obvious the rim feature will be. It indicates that there is an inevitable connection between material ablation and the formation of raised rim, however which was not studied before. And it can't be reasonably explained only by experiments. Therefore, it is necessary to carry out systematic research on surface topography evolution of the mitigated pit and intrinsic physical mechanism during the laser interaction with fused silica through numerical simulation. These contents will be elaborated in Sections "Modeling of localized CO_2 laser mitigation" and "Results and discussions".

The sizes of mitigated pits under different laser powers are shown in Fig. 4.

It can be seen that as the laser power increases, the depth of the mitigated pits increases exponentially. When the laser power exceeds 29 W, the depth of the mitigated pit increases sharply due to the occurrence of material ablation. The relationship between material ablation and the surface topography evolution will be further studied next. By fitting the data points, the lateral dimension increases linearly with the increase of laser power. This indicates that a slight change in laser power will cause a large variation in depth of the mitigated pit under the same laser irradiation time. Thus, the stability of the laser power is extremely important in the process of laser damage mitigation process.

Modeling of localized CO_2 laser mitigation

Mathematical model

Physical model and assumptions

The schematic of localized CO_2 laser mitigation of surface damage on fused silica optics is shown in Fig. 5. The thermo-mechanical interaction between CO_2 laser and fused silica, which involves heat transfer, fluid flow and evaporation ablation, is a multi-physics coupling process. When the surface damage site is irradiated by CO_2 laser beam, the temperature of fused silica rises rapidly over melting point and the molten pool will be formed. Then, the melted material tends to redistribute to heal the cracks at the bottom of the damage site and to flow outwards. Simultaneously, evaporation ablation occurs when the substrate temperature exceeds vaporization point. The vaporization recoil pressure induced by escaping silica vapor acts on the surface of the molten pool, which further causes material to flow outwards and sequentially accumulate around the damage site. The final surface topography with the feature of deep crater and raised rim largely depends on the hydrodynamic evolution of the free surface during the laser damage mitigation process.

In order to comprehensively study the surface topography evolution and intrinsic physical mechanism during CO_2 laser mitigation surface damage of fused silica optics, a mathematical model has been established based on the following assumptions:

(1) The fused silica material is homogeneous and isotropic.
(2) Flowing fluid is treated as an incompressible Newtonian fluid, and only laminar flow is considered.
(3) The problems including fluid flow and heat transfer are mainly concentrated on the characterization of solid-liquid phase conversion. The third phase (fused silica vapor) has been included in the boundary conditions.
(4) Laser energy absorbed by the substrate is considered to be a surface

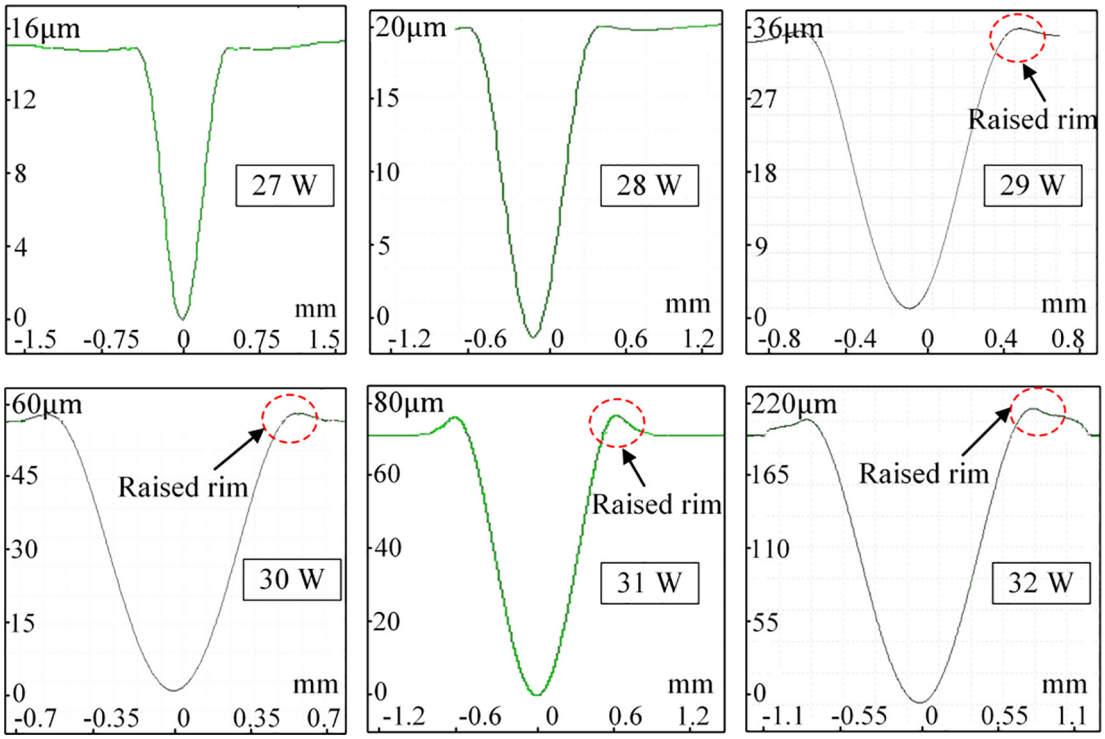

Fig. 3. The profiles of the mitigated pits under different laser powers measured by Taylor Hobson profiler.

heat flux rather than a volumetric heat source.

(5) Fused silica vapor is treated as an ideal gas, ignoring the absorption of laser energy by the sprayed exhalation.

Governing equations

The temperature field can be obtained by solving the following equation [30]:

$$\rho C_p \frac{\partial T}{\partial t} + \rho C_p(\vec{u}\cdot\nabla T) = \nabla\cdot(k\nabla T) \tag{1}$$

where ρ is the density, T is the absolute temperature, k is the thermal conductivity, $C_p$is the heat capacity and $\vec{u}$ represents the flow velocity, which can be solved by the Navier-Stokes equation [32]:

$$\rho\frac{\partial \vec{u}}{\partial t} + \rho(\vec{u}\cdot\nabla)\vec{u} = \nabla\cdot[-pI + \mu(\vec{\nabla}\vec{u}) + (\vec{\nabla}\vec{u})^T] - \rho(1-\beta(T-T_m))\vec{g} + \vec{F} \tag{2}$$

where p is the pressure, μ is the dynamic viscosity, β is the thermal expansion coefficient, T_m is the melting temperature, I is identity

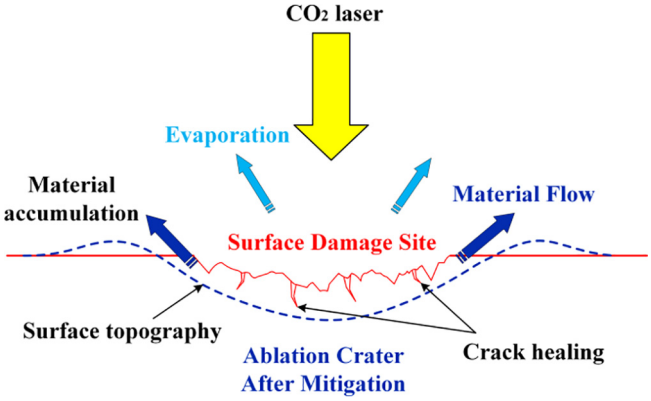

Fig. 5. The schematic of localized CO_2 laser mitigation of surface damage.

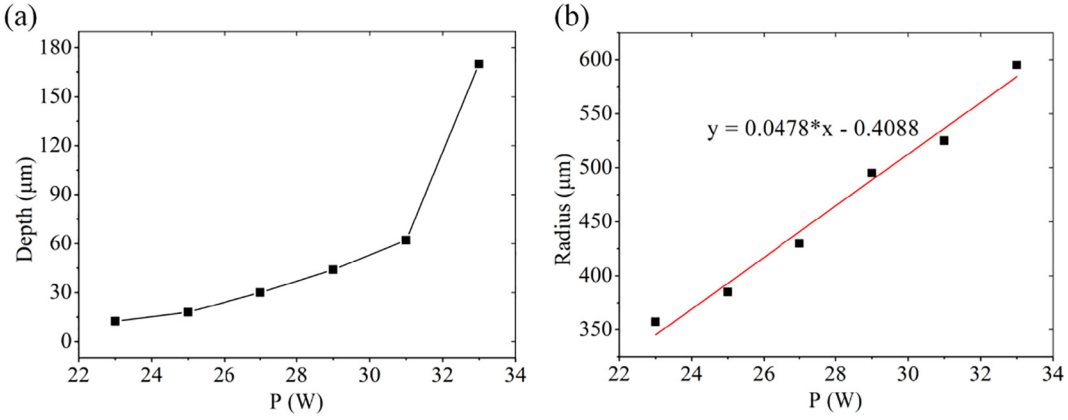

Fig. 4. The sizes of mitigated pits under different laser powers. (a) The curve of mitigation pit depth; (b) The curve of mitigation pit radius.

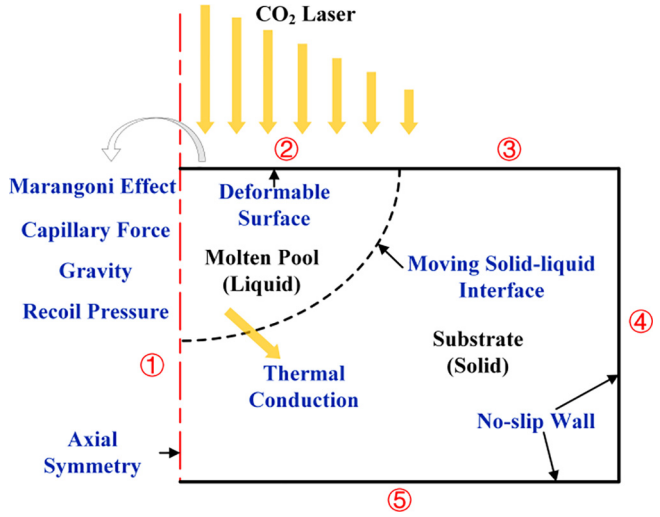

Fig. 6. The geometric model of CO_2 laser interaction with fused silica.

matrix, $\vec{g}$ is the gravity acceleration. $\vec{F}$ is the Darcy damping force, which can be defined as:

$$\vec{F} = -C\frac{(1-f_l)^2}{(f_l^3+b)}\vec{u} \tag{3}$$

$$f_l = \begin{cases} 0, & T \leqslant T_s \\ \frac{T-T_s}{T_l-T_s}, & T_s \leqslant T \leqslant T_l \\ 1, & T > T_l \end{cases} \tag{4}$$

where b is a coefficient to avoid the division by zero, T_s and T_l represent solidus and liquidus temperatures, respectively.

For incompressible flow, the continuity equation is expressed as:

$$\rho\nabla\cdot(\vec{u}) = 0 \tag{5}$$

Numerical model

Geometry

In order to save computing resources and reduce calculation time, two-dimensional axisymmetric geometry is regarded as the computational domain, which is shown in Fig. 6. The calculation model is established based on the fluid control equation, heat and mass transfer equation and material phase transition kinetics, which consider the effects of Marangoni convection, gravity, capillary force and vaporization recoil pressure, as well as the nonlinear variation of material physical parameters with respect to temperature.

Boundary conditions

All boundary conditions of the computational domain are marked in Fig. 6. In terms of heat transfer, boundary 1 is the symmetry axis. The conditions of boundary 2 are laser heat flux, heat convection and heat radiation, which are described below:

$$-k\nabla T = \alpha I - h[T - T_{amb}] - \varepsilon B[T^4 - T_{amb}^4] \tag{6}$$

where h is the natural convection coefficient, ε is the emissivity, B is the Stefan–Boltzmann constant, T_{amb} is the ambient temperature, and I is the laser intensity with gaussian distribution, which is defined as:

$$I = \alpha\frac{(1-\varphi)P}{\pi r^2} * \exp(-\frac{2(x^2+y^2)}{r^2}) * \exp(-\alpha z) \tag{7}$$

where P is the laser power, r is the laser beam radius, φ is the Fresnel reflection coefficient, α is the laser absorption coefficient, calculated from the equation below.

$$\alpha = \frac{4\pi n_k}{\lambda} \tag{8}$$

where n_k and λ represent the imaginary part of the refractive index and the laser wavelength, respectively.

Boundary 3 and boundary 4 are considered to the heat losses of convection and radiation, controlled by follow equation:

$$-k\nabla T = h[T - T_{amb}] + \varepsilon\sigma\ [T^4 - T_{amb}^4] \tag{9}$$

While boundary 5 is treated as thermal insulation, expressed as:

$$\nabla T = 0 \tag{10}$$

In terms of fluid flow, boundary 2 is defined as a freely deformed surface. On this surface, the thermal capillary force (Marangoni effect) acts on the tangential direction, which is related to the temperature gradient. While the capillary force acts on the normal direction, and its strength is proportional to the curvature of the surface profile. In this work, surface tension is a function of temperature that can be expressed as:

$$\sigma = \sigma_0 - \gamma(T - T_m) \tag{11}$$

where σ_0 is the surface tension coefficient, γ is the temperature derivative of surface tension, T_m is the melting temperature.

The normal component of surface tension can be expressed as:

$$\vec{\sigma_n} = \kappa\sigma\cdot\vec{n} \tag{12}$$

While in the tangential direction,

$$\vec{\sigma_t} = \frac{\partial\sigma}{\partial T}\nabla_s T\cdot\vec{t} \tag{13}$$

Eqs. (12) and (13) represent the capillary force and the thermal capillary force, respectively. Where κ is the curvature of surface profile, $\nabla_s T$ is the temperature gradient.

Boundaries 3,4,5 are set for no-slip wall.

When the substrate temperature exceeds the vaporization point, evaporation ablation of fused silica material occurs, and the vaporized particles carry away a part of the heat flux, which can be expressed as [33]

$$qevap = M_v \times L_v \tag{14}$$

where L_v is the latent heat of vaporization, and M_v is the mass flow rate of vapor, which is a function of surface temperature T, and can be described as follow:

$$M_v = \sqrt{\frac{m}{2\pi k_b T}} \times P_{sat}(T) \times (1-\beta_r) \tag{15}$$

where m is the atomic mass, k_b is the Boltzmann constant, β_r is the diffusion coefficient, taking $\beta_r = 0.17$, P_{sat} is the vapor pressure, which is given by

$$P_{sat}(T) = P_{atm} \times \exp\left(\frac{M_a L_v}{R}\left(\frac{1}{T_v} - \frac{1}{T}\right)\right) \tag{16}$$

where M_a is the molecular mass, R is the ideal gas constant, T_v is the evaporation temperature, P_{atm} is the standard atmospheric pressure. The vaporization recoil pressure can be expressed as:

$$P_{recoil} = \begin{cases} P_{atm}, & 0 \leqslant T < T_v \\ \frac{1+\beta_r}{2} \times P_{sat}(T), & T \geqslant T_v \end{cases} \tag{17}$$

All the boundary conditions are listed in Table 1.

Properties of fused silica and parameters of model

During CO_2 laser irradiation, the computational model takes the nonlinear variation of material physical properties with respect to temperature into consideration, such as the heat conductivity $K(T)$ [34], heat capacity $C_p(T)$ [30], and dynamic viscosity $\eta(T)$ [35], as shown in Fig. 7.

Table 1
Boundary conditions of numerical model of CO_2 laser interaction with fused silica.

Physics	Physical condition	Boundary	Boundary condition
Heat transfer	Laser irradiation	2	Heat flux
	Natural convection	2,3,4	Convection
	Radiation	2,3,4	Diffuse surface
	Insulation	5	Thermal insulation
Fluid flow	Normal stress	2	Capillary force
	Tangential stress	2	Marangoni effect
	Recoil pressure	2	Vaporization recoil pressure
	Wall	3,4,5	No-slip wall
	Axis	1	Axial symmetry

As shown in Eqs. (1) and (2), thermal conductivity and heat capacity are key parameters in heat transfer calculation, while dynamic viscosity directly affects the characteristics of fluid flow. In this work, numerical model has taken bidirectional coupling between properties of fused silica and temperature into consideration. Other physical properties of fused silica used in this work are shown in Table 2.

The laser used in simulation is CW CO_2 laser with wavelength of 10.6 μm, spatial Gaussian distribution, and spot diameter of about 2 mm at $1/e^2$. The laser power is set to be 28 W, and the irradiation time is 10 s. CO_2 laser parameters and constants used for simulation are listed in Table 3.

Table 2
Properties of fused silica.

Property (unit)	Symbol	Value	Reference
Melting temperature (K)	T_m	2273	[36]
Evaporation temperature (K)	T_v	2973	[36]
Density (kg/m^3)	ρ	2201	[36]
Latent heat of melting (J/kg)	L_m	1.23×10^5	[37]
Latent heat of evaporation (J/kg)	L_v	1.14×10^7	[27]
Laser absorption coefficient	α	0.8	[28]
Radiation emissivity	ε	0.8	[37]
Surface tension coefficient (N/m^2)	σ_0	0.38	[32]
Temperature derivative of surface tension (N/(m·K))	$\partial\sigma/\partial T$	-6×10^{-5}	[32]
Molecular weight (g/mol)	M	40	[26]
Thermal expansion coefficient (K^{-1})	β	5×10^{-7}	[26]

Table 3
CO_2 laser parameters and constants used for simulation.

Parameter(unit)	Symbol	Value
Laser power (W)	P	28
Beam size (mm)	r	2
Ambient temperature (K)	T_{amb}	297.15
Ambient atmospheric pressure (N/m^2)	P_{amb}	101,300
Stefan–Boltzmann constant (W/(m^2·K^4))	σ	5.67×10^{-8}
Ideal gas constant (J/ (mol ·K))	R	8.314
Gravity acceleration (m/s^2)	g	9.81

Results and discussions

Temperature fields of fused silica during CO_2 laser irradiation

When CW CO_2 laser irradiates the surface of fused silica, the temperature of substrate increases gradually with the laser energy absorbed by material. As the laser irradiation time increases to 1.3 s, the center temperature of substrate exceeds the melting temperature of 2273 K. Then the center material begins to melt, and the melted region expands to the inside of the bulk material as the laser keeps on acting. When the surface temperature reaches to the evaporation point of 2973 k at the laser heating time of 6.5 s, the central material begins to undergo evaporation and ablation, the area of which gradually increases. The distributions of temperature field at various heating times are shown in Fig. 8(a)–(c).

The temperature distributions during cooling stage are shown in Fig. 8(d)–(f). It can be seen that when the laser is off, the substrate temperature decreases sharply due to the huge heat dissipation of convection and radiation between substrate and surroundings. Soon, the substrate temperature is completely below the melting point and the molten region disappears at the cooling time of 0.13 s.

Surface topography evolution and intrinsic physical mechanism during laser damage mitigation process

From above analysis of temperature distribution, the substrate undergoes the processes of heating, melting, evaporation, cooling, and solidification throughout the laser action. Fig. 9 shows the process of material phase transition during laser heating and cooling. The white arrows in figures indicate the velocity vector. It can be seen that the molten region of the substrate expands and the solid-liquid phase interface continuously moves to the inside of the bulk as the temperature increases. At the same time, the effects of Marangoni convection and the thermal capillary force increase due to the rising of tangential temperature gradient. However, the surface deformation of the molten region caused by the Marangoni effect is very small because of the large viscosity of fused silica, as shown in Fig. 9(a). As the evaporation and ablation of the central material occur, the resulting vaporization recoil pressure acts perpendicularly on the surface of the molten region,

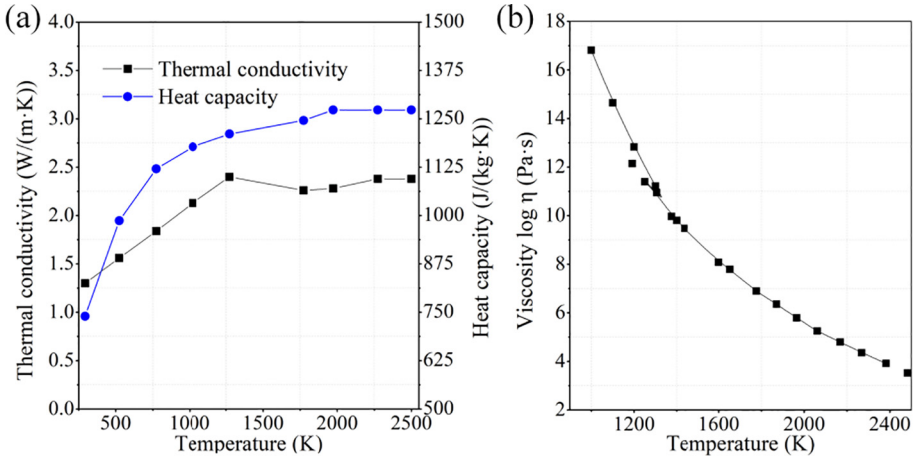

Fig. 7. Temperature dependent material properties of fused silica. (a) Heat capacity and thermal conductivity; (b) Dynamic viscosity.

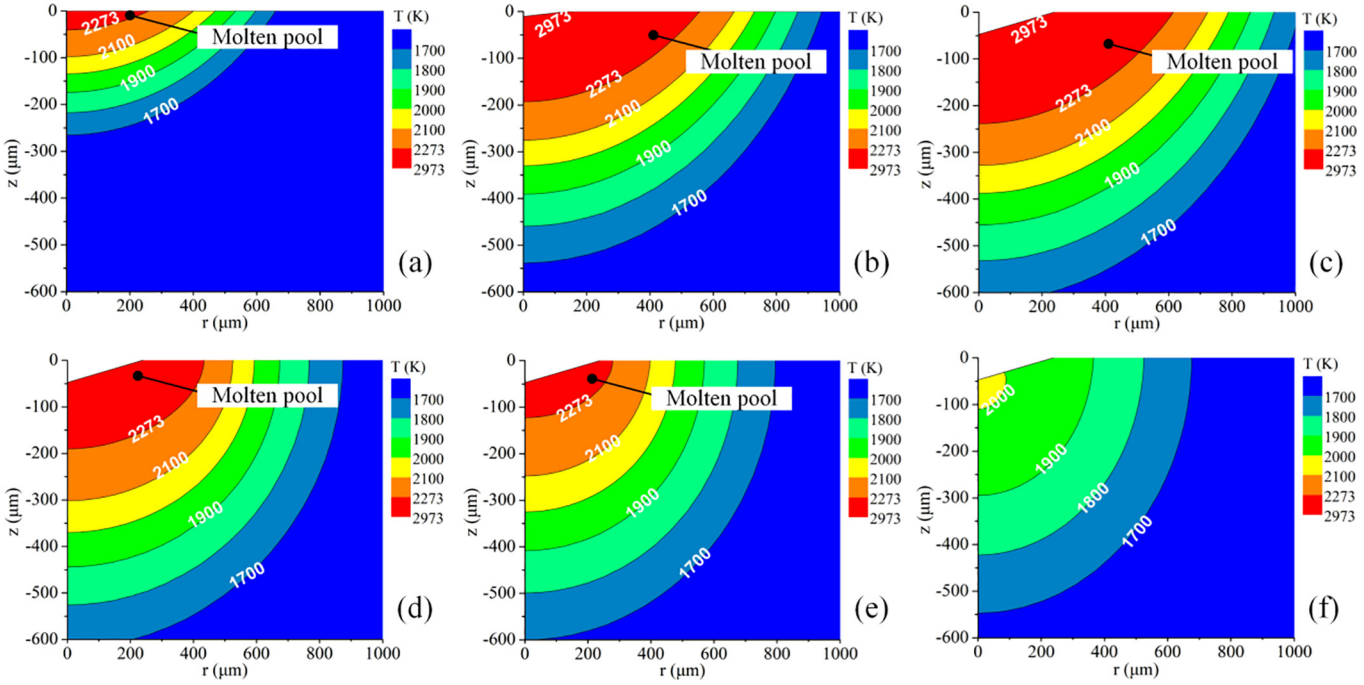

Fig. 8. The distributions of temperature field during laser heating and cooling processes. (a) Heating for 1.3 s; (b) Heating for 6.5 s; (c) Heating for 10 s; (d) Cooling for 0.05 s; (e) Cooling for 0.1 s; (f) Cooling for 0.13 s.

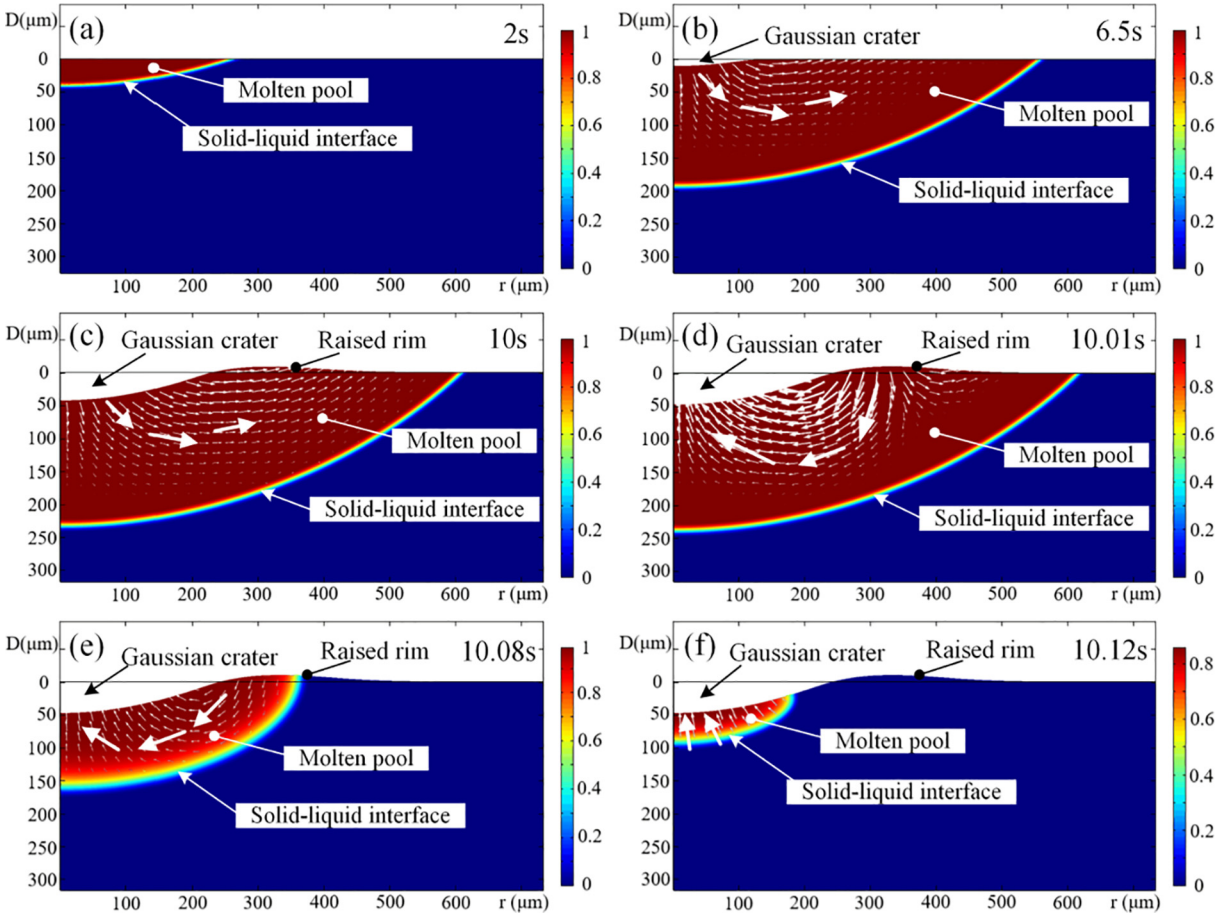

Fig. 9. The process of phase transition during laser heating and cooling processes. (a) Heating for 2 s; (b) Heating for 6.5 s; (c) Heating for 10 s; (d) Cooling for 0.01 s; (e) Cooling 0.08 s; (f) Cooling for 0.12 s.

which is much larger than the thermal capillary force. The molten material begins to move outwards from the center under the combined effects of vaporization recoil pressure, Marangoni effect and gravity. However, since the viscosity of fused silica increases rapidly along the radial direction, the outward material accumulates at the periphery to form a raised rim, and the central region appears a Gaussian pit topography, as shown in Fig. 9(b). Accompanied with the formation of the crater with raised rim, the capillary force begins to act inside the molten pool, and its strength is proportional to the curvature of the surface profile. The direction of capillary force is downward for the negative curvature surface and upward for the positive curvature surface, which hinders the surface deformation of the molten pool. As the laser irradiation time increases, the solid-liquid phase interface keeps moving to inside, and the material of central region continues to be ablated and to move outwards. The depth of the crater and the height of the raised rim become larger and larger, meanwhile the capillary force generated by the increasing of surface curvature also becomes non-negligible, which has a certain hindrance to the outward movement of material. However, the velocity vector is still outward since the capillary force is still smaller than the vaporization recoil pressure, as shown in Fig. 9(c). When the laser shutting down, the substrate temperature sharply decreases below the evaporation temperature, and the vaporization recoil pressure disappears. At this time, the direction of capillary force in the raised region is downward, while the capillary force in the bottom of the crater is upward. Therefore, the molten material has a tendency to flow back from the height under the action of the capillary force, so the velocity vector is inward. However, the capillary force is too small to change the surface topography, as shown in Fig. 9(d). On the other hand, the solid-liquid phase interface moves outwards from inside of the bulk rapidly, and the area capillary force acting on becomes smaller and smaller until the molten region disappears completely, as shown in Fig. 9(e) and (f).

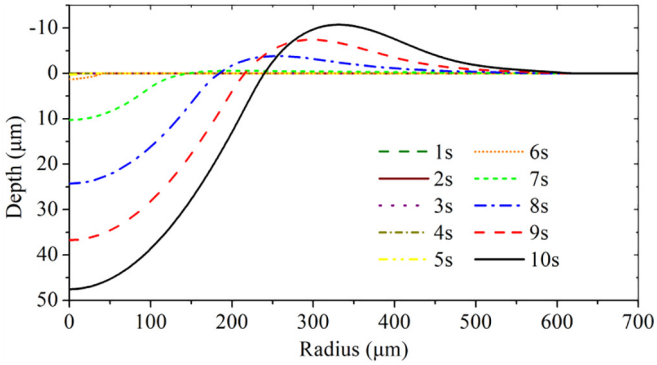

Fig. 11. The evolution curves of surface topography during CO_2 laser irradiation for 10 s. The applied laser power is 28 W, and laser beam diameter is 2 mm.

The solid-liquid phase interfaces at different times during the laser heating and cooling stages are extracted as shown in Fig. 10.

It can be seen from Fig. 10(a) and (b) that the speed of the solid-liquid phase interface moving inwards decreases gradually during the laser heating time varying from 1 s to 10 s. It is because that the heat absorbed by substrate from the laser reduces as the depth increases. As a result, the melting rate of the material gets slower and slower as shown in Eq. (7). Moreover, the variation range of the radial position of the solid-liquid phase interface is larger than that of the depth position. Nevertheless, the growth rates of radial and depth positions both get more and more gentle.

It can be seen from Fig. 10(c) and (d) that the speed of the solid-liquid phase interface moving outwards increases gradually during the cooling time varying from 0 s to 0.13 s after laser shutting down. It indicates that the cooling rate is getting faster and faster. The reason is

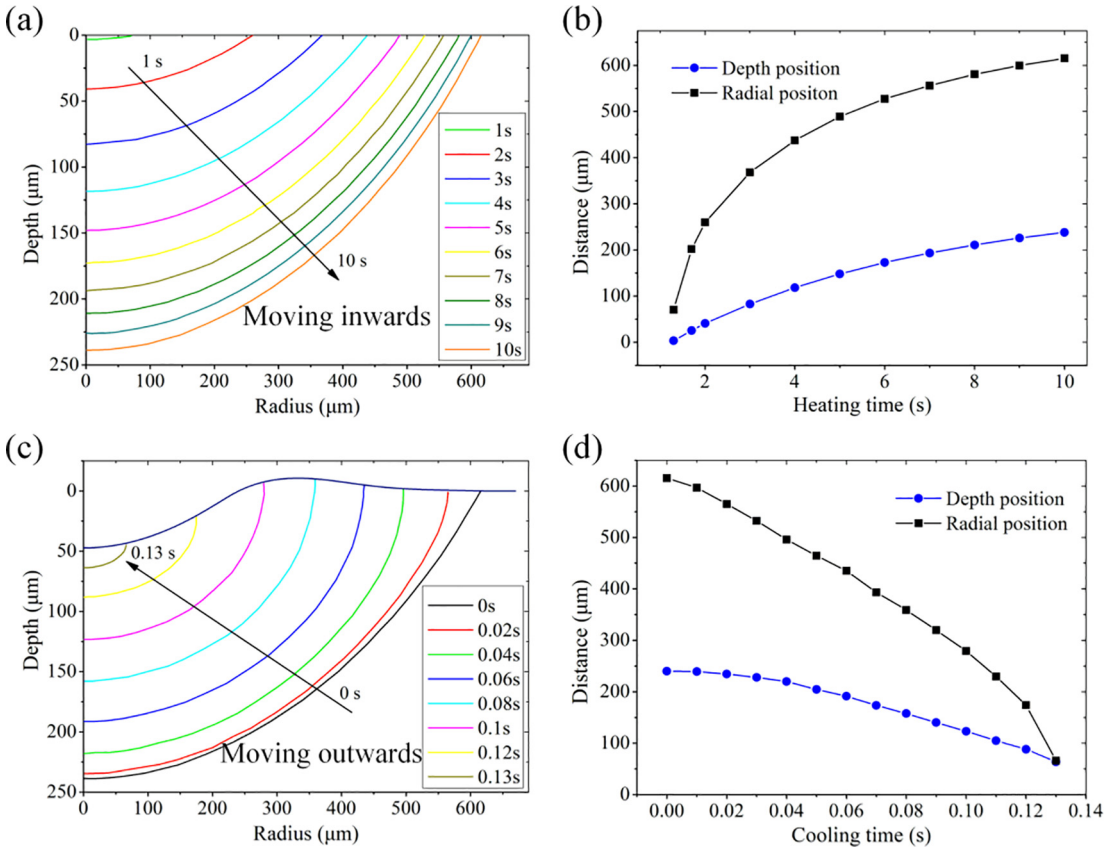

Fig. 10. The distributions of solid–liquid phase interface at different times during laser heating and cooling stages. (a) (c) Solid-liquid phase interface; (b) (d) Radial and depth position of solid-liquid phase interface. (a) and (b) are in case of heating stage; (c) and (d) are in case of cooling stage.

that the closer the molten region is to the surface, the faster the heat dissipation is. This phenomenon is exactly the opposite case of the laser heating process. Additionally, the radial and depth positions of the solid-liquid phase interface decrease more and more rapidly. The variation range of radial position is also larger than that of the depth direction.

Fig. 11 shows the evolution curves of the surface topography of the fused silica under the irradiation of CO_2 laser. It can be seen that the surface is almost free of deformation at initial stage of laser heating. When the heating time exceeds 6 s, both the depth of the crater and the height of raised rim increase gradually. Meanwhile, the position of maximum bulge moves to the outside, and a Gaussian crater is formed. The intrinsic mechanism of its formation can be observed in Fig. 9.

It can be concluded from above analysis that the material ablation and the formation of raised rim occur simultaneously due to the dominant factor of vaporization recoil pressure, which is exactly the same as the experimental conclusions shown in Fig. 2. Additionally, the more severely the material ablation occurs, the greater the vaporization recoil pressure gets, and the more obviously the rim feature appears. It also can be concluded that in addition to material ablation removal, the sharp increase of vaporization recoil pressure along with ablation is another reason for the abrupt growth of the depth of mitigated pit. The simulation results are good indication of the underlying causes of this phenomenon. On the other hand, the evolutions of surface Gaussian topography are also consistent with experimental observations shown in Fig. 3. However, the larger raised rim feature will cause strong light field distortion and local light intensification, leading to the component itself to be damaged again under the irradiation of subsequent laser. Therefore, the most basic method to improve the laser damage threshold of fused silica is reducing material ablation during laser mitigation process. According to above analysis, a lower laser power with longer action time or variable laser power at different stages are preferred in practical localized CO2 laser repairing of surface damage. On the other hand, the laser power and laser action time should be selected under the premise of completely removing the damage pit and surrounding cracks. It also needs to ensure that there are not bubbles appeared in the bottom of the mitigated crater, and the heat affected zone will not has an effect on the laser damage threshold of the optics.

Evolutions of surface topography and solid-liquid phase interface during laser heating time from 7 s to 10 s are illustrated in Fig. 12. It can be seen that the descending depth d_1 of the Gaussian crater is smaller than the moving depth d_3 of the solid-liquid phase interface. The reason is that a part of material at the bottom of the crater is ablated by evaporation. The moving distance d_2 of the raised rim is approximately twice the moving distance d_4 of solid-liquid phase interface. This is because the heating efficiency at the edge of the Gaussian laser beam is much lower than that at the center, while the effect of the vaporization recoil pressure at the central region remains constant. In other words, the melting rate of the substrate is reduced, while the speed at which the material flows outwards does not change a lot. The resulting maximum height of the raised rim h is 10.7 μm. The figure embedded in Fig. 12 is the curves of the height and radial positions of raised rim versus time. It can be seen that the height of the raised rim increases linearly with time from 7 s to 10 s, while the increasing speed of the radial position of the maximum bulge gets more and more gentle, which is related to the expansion speed of the molten pool.

Melt flow of fused silica interaction with CO_2 laser

The velocity fields of the molten pool during laser heating and cooling processes are shown in Fig. 13. It can be seen that the flow velocity gets larger and larger with laser irradiation. In the initial stage, the velocity is only 10^{-8} m/s orders of magnitude, its direction is outward due to the effect of the thermal capillary force, as shown in Fig. 13(a). Then, the velocity rapidly increases to 10^{-6} m/s orders of magnitude under the combined actions of vaporization recoil pressure and thermal capillary force, its direction is still outward, as shown in Fig. 13(b) and (c). Fig. 13(d)–(f) illustrate the velocity fields after laser shutting down. The molten material has a tendency to reflow because of the capillary force, and the velocity vector is inward. Besides, the velocity is reduced from 10^{-6} m/s orders of magnitude to 10^{-8} m/s after laser shutting down, which is too small to change the surface topography.

From above analysis, the maximum velocity and its radial and depth positions constantly change during the whole process, both of which are plotted in Fig. 14. It can be seen from Fig. 14(a) that the maximum velocity increases slowly in the initial stage. As laser heating for 6 s, the maximum velocity increases rapidly due to the action of vaporization recoil pressure on the surface of molten pool, and then it remains constant after heating time of 7 s. The radial position of the maximum velocity decreases rapidly at 6 s, then gradually increases from 6.5 s. While the depth position of the maximum velocity decreases rapidly from 6 s to 7 s, then remains stable. The reason of these variations is that the maximum velocity appears at the edge of Gaussian crater due to the action of vaporization recoil pressure from about 6 s. As the Gaussian crater expanding and material flowing outwards, the position where the maximum velocity occurs also moves outwards, which always appears near the edge of the crater.

It can be seen from Fig. 14(b) that the maximum velocity firstly decreases rapidly during the cooling time of 0 to 0.03 s. Then, the maximum velocity tends to zero slowly. Meanwhile, the radial and depth positions of the maximum velocity decrease rapidly, which indicates that the maximum velocity moves from the edge of the Gaussian crater to the bottom. However, there is a slight fluctuation in the radial

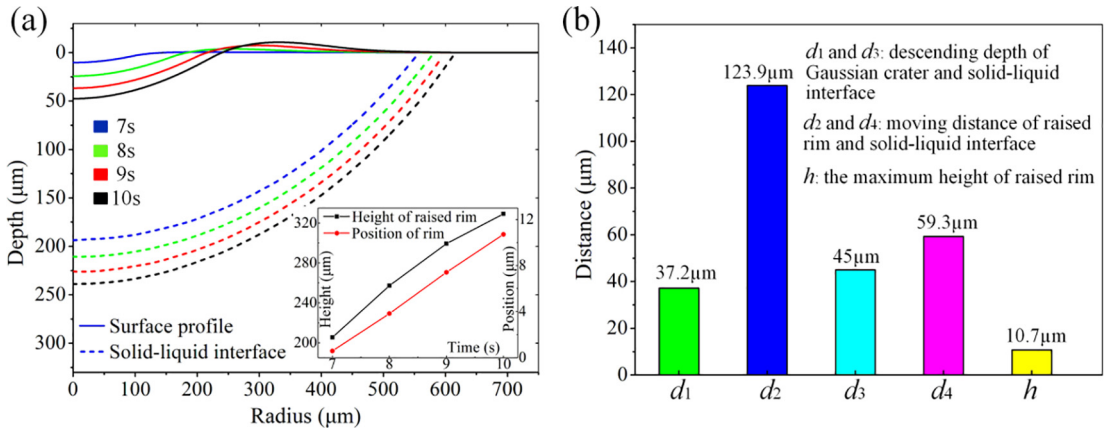

Fig. 12. Evolutions of the surface topography and the solid–liquid phase interface during laser heating time from 7 s to 10 s. (a) The curves of surface topography and the solid–liquid phase interface; (b) Statistical values of each variable.

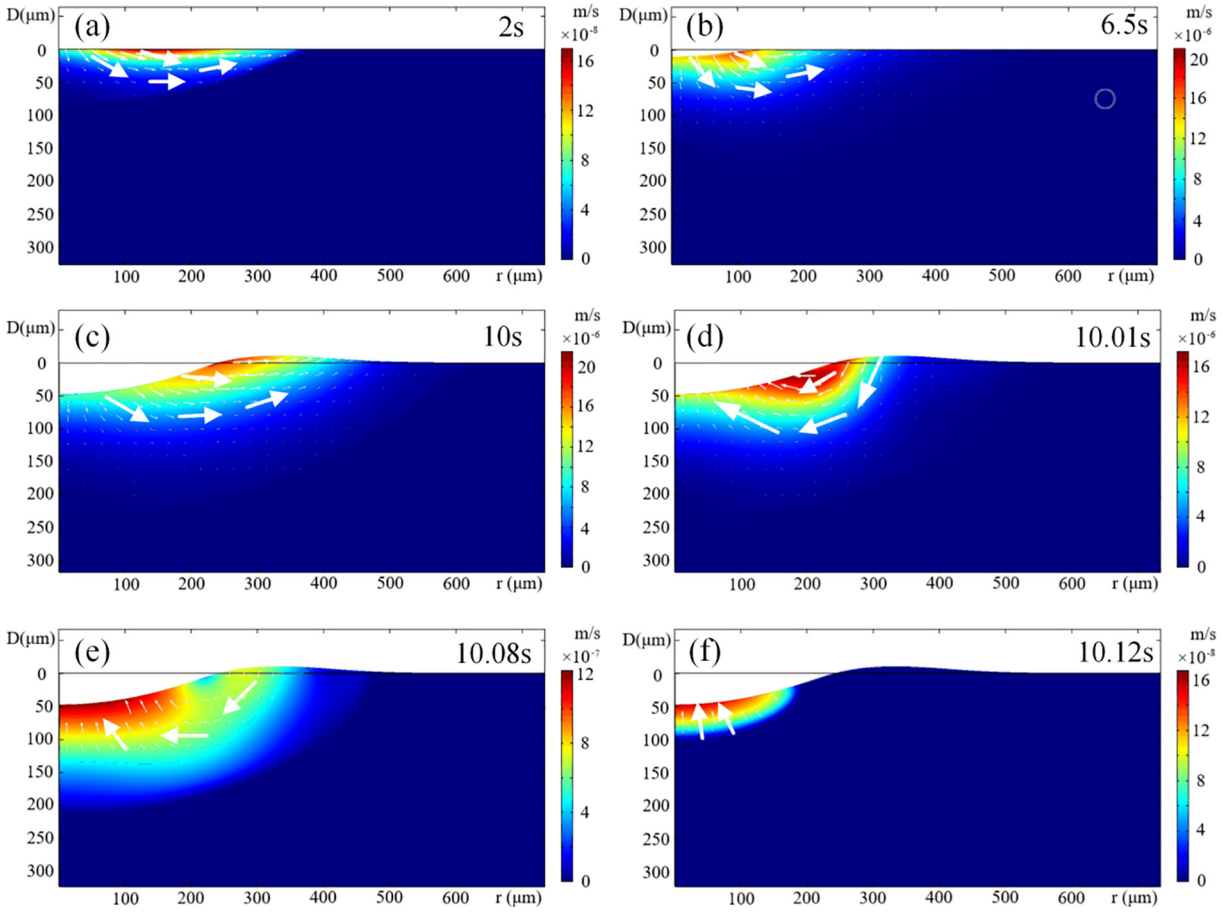

Fig. 13. The velocity fields of the molten pool during laser heating and cooling processes. (a) Heating for 2 s; (b) Heating for 6.5 s; (c) Heating for 10 s; (d) Cooling for 0.01 s; (e) Cooling for 0.08 s (f) Cooling for 0.12 s.

and depth positions during the cooling time of 0.06 to 0.11 s, which may be the result of the interaction of the capillary force and the temperature gradient.

Conclusion

In this work, the surface topography evolution and intrinsic physical mechanism of localized CO_2 laser repairing of surface damage on fused silica optics are investigated by means of experiments and numerical simulations. The influence law between various intrinsic factors during different stages of laser interaction with fused silica is also obtained. The conclusions can be drawn below:

(1) As the laser power increases, the material ablation and the formation of raised rim occur simultaneously. The depth of the mitigated crater increases sharply from 29 W, while the lateral dimension increases linearly. Thus, the stability of the laser power is extremely important in the practical CO_2 laser mitigation process.
(2) Substrate temperature increases gradually during laser heating process, while it decreases sharply after laser shutting down. The fused silica undergoes the processes of heating, melting, evaporation, cooling, and solidification throughout the laser mitigation process.
(3) The vaporization recoil pressure is the dominant factor for forming a Gaussian crater with a raised rim feature, which could be a good explanation for the phenomena observed in the experiments. The capillary force causes the material at the edge of the molten pool to have a tendency to reflow after laser shutting down, but it is too small to change the surface topography.
(4) The speed of the solid-liquid phase interface moving inward decreases gradually with heating time, while the speed moving outwards increases during cooling time. The variation range of the radial position of the solid-liquid phase interface is larger than that of the depth position.
(5) The outward flow velocity of the molten pool increases rapidly to 10^{-6} m/s under the combined action of vaporization recoil pressure and thermal capillary force, which is much larger than the reflow velocity. The maximum velocity and its position change constantly during the whole process.

CRediT authorship contribution statement

Chao Tan: Methodology, Investigation, Writing - original draft. **Linjie Zhao:** Software, Validation. **Mingjun Chen:** Supervision. **Jian Cheng:** Writing - review & editing. **Chunya Wu:** Visualization. **Qi Liu:** Data curation. **Hao Yang:** Data curation. **Zhaoyang Yin:** Formal analysis. **Wei Liao:** Resources.

Declaration of Competing Interest

The authors declare that they have no known competing financial interests or personal relationships that could have appeared to influence the work reported in this paper.

Acknowledgments

This work was supported by the National Natural Science Foundation of China (Grant Nos. 51775147, 51705105); Science

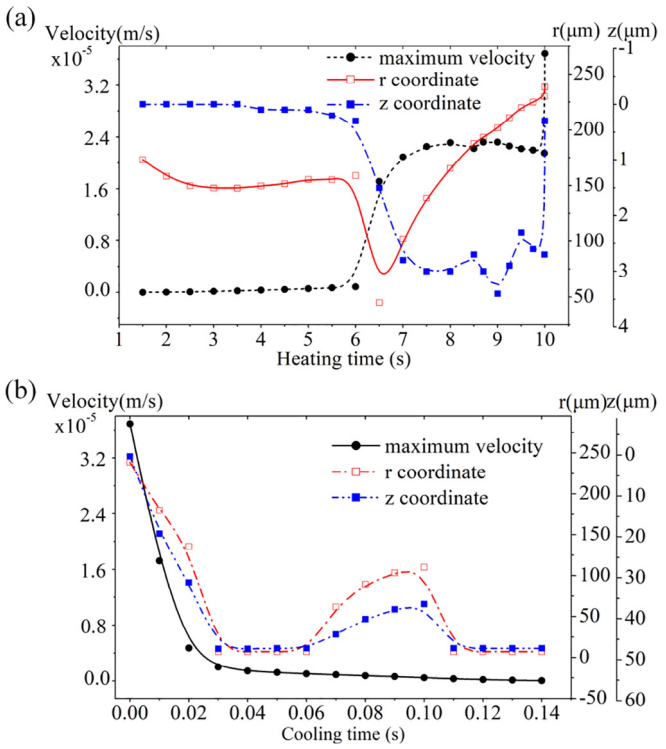

Fig. 14. Evolutions of maximum velocity and its positions during laser heating and cooling stages. (a) is in case of heating stage, and (b) is in case of cooling stage.

Challenge Project (Grant No. TZ2016006-0503-01); Young Elite Scientists Sponsorship Program by CAST (No. 2018QNRC001), China Postdoctoral Science Foundation funded project (Grant Nos. 2018T110288, 2017M621260); Self-Planned Task (Grant Nos. SKLRS201718A, SKLRS201803B) of State Key Laboratory of Robotics and System (HIT).

References

[1] Heidrich S, Richmann A, Schmitz P, Willenborg E, Wissenbach K, Loosen P, et al. Optics manufacturing by laser radiation. Opt Lasers Eng 2014;59:34–40.
[2] Sohn I-B, Choi H-K, Noh Y-C, Lee M-S, Oh J-K, Kim S-M, et al. Performance analysis of CO_2 laser polished angled ribbon fiber. Opt Fiber Technol 2017;33:77–82.
[3] Sohn I-B, Choi H-K, Noh Y-C, Kim J, Ahsan MS. Laser assisted fabrication of micro-lens array and characterization of their beam shaping property. Appl Surf Sci 2019;479:375–85.
[4] Wlodarczyk KL, Weston NJ, Ardron M, Hand DP. Direct CO_2 laser-based generation of holographic structures on the surface of glass. Opt Express 2016;24:1447–62.
[5] He T, Wei C, Jiang Z, Zhao Y, Shao J. Super-smooth surface demonstration and the physical mechanism of CO2 laser polishing of fused silica. Opt Lett 2018;43:5777–80.
[6] Mendez E, Nowak K, Baker H, Villarreal F, Hall D. Localized CO_2 laser damage repair of fused silica optics. Appl Opt 2006;45:5358–67.
[7] Bass IL, Guss GM, Nostrand MJ, Wegner PJ. An improved method of mitigating laser-induced surface damage growth in fused silica using a rastered pulsed CO_2 laser. Laser-Induced Damage in Optical Materials: 2010, International Society for Optics and Photonics. 2010. p. 784220.
[8] Yang ST, Matthews MJ, Elhadj S, Cooke D, Guss GM, Draggoo VG, et al. Comparing the use of mid-infrared versus far-infrared lasers for mitigating damage growth on fused silica. Appl Opt 2010;49:2606–16.
[9] Zhang C, Zhang L, Jiang X, Jia B, Liao W, Dai R, et al. Influence of pulse length on heat affected zones of evaporatively-mitigated damages of fused silica optics by CO_2 laser. Opt Lasers Eng 2020;125:105857.
[10] Cormont P, Bourgeade A, Cavaro S, Donval T, Doualle T, Gaborit G, et al. Relevance of carbon dioxide laser to remove scratches on large fused silica polished optics. Adv Eng Mater 2015;17:253–9.
[11] Cormont P, Combis P, Gallais L, Hecquet C, Lamaignère L, Rullier JL. Removal of scratches on fused silica optics by using a CO_2 laser. Opt Express 2013;21:28272–89.
[12] Palmier S, Gallais L, Commandré M, Cormont P, Courchinoux R, Lamaignère L, et al. Optimization of a laser mitigation process in damaged fused silica. Appl Surf Sci 2009;255:5532–6.
[13] Matthews MJ, Yang ST, Shen N, Elhadj S, Raman RN, Guss G, et al. Micro-shaping, polishing, and damage repair of fused silica surfaces using focused infrared laser beams. Adv Eng Mater 2015;17:247–52.
[14] Spaeth M, Wegner P, Suratwala T, Nostrand M, Bude J, Conder A, et al. Optics recycle loop strategy for NIF operations above UV laser-induced damage threshold. Fusion Sci Technol 2016;69:265–94.
[15] Doualle T, Gallais L, Monneret S, Bouillet S, Bourgeade A, Ameil C, Lamaignère L, Cormont P. Development of a laser damage growth mitigation process, based on CO_2 laser micro processing, for the Laser MegaJoule fused silica optics. Laser-Induced Damage in Optical Materials 2016, International Society for Optics and Photonics. 2016. p. 1001407.
[16] Zheng W, Wei X, Zhu Q, Jing F, Hu D, Su J, et al. Laser performance of the SG-III laser facility. High Power Laser Sci Eng 2016;4.
[17] Dai W, Xiang X, Jiang Y, Wang H, Li X, Yuan X, et al. Surface evolution and laser damage resistance of CO_2 laser irradiated area of fused silica. Opt Lasers Eng 2011;49:273–80.
[18] Gallais L, Cormont P, Rullier J-L. Investigation of stress induced by CO_2 laser processing of fused silica optics for laser damage growth mitigation. Opt Express 2009;17:23488–501.
[19] Gao X, Jiang Y, Qiu R, Zhou Q, Zuo R, Zhou G, et al. Effect of the repaired damage morphology of fused silica on the modulation of incident laser. Opt Mater 2017;64:295–301.
[20] Matthews MJ, Shen N, Honig J, Bude JD, Rubenchik AM. Phase modulation and morphological evolution associated with surface-bound particle ablation. JOSA B 2013;30:3233–42.
[21] Elhadj S, Matthews MJ, Yang ST. Combined infrared thermal imaging and laser heating for the study of materials thermophysical and processing properties at high temperatures. Crit Rev Solid State Mater Sci 2014;39:175–96.
[22] Doualle T, Gallais L, Cormont P, Donval T, Lamaignère L, Rullier J. Effect of annealing on the laser induced damage of polished and CO_2 laser-processed fused silica surfaces. J Appl Phys 2016;119:213106.
[23] Cormont P, Gallais L, Lamaignère L, Rullier JL, Combis P, Hebert D. Impact of two CO_2 laser heatings for damage repairing on fused silica surface. Opt Express 2010;18:26068–76.
[24] Fang Z, Zhao YA, Sun W, Li Z, Hu G, Liu X, Li D, Shao J. CO_2 laser mitigation of the ultraviolet laser damage site on a fused silica surface. Opt Eng 2014;53:084107.
[25] Doualle T, Ollé A, Cormont P, Monneret S, Gallais L. Laser-induced birefringence measurements by quantitative polarized-phase microscopy. Opt Lett 2017;42:1616–9.
[26] Robin L, Combis P, Cormont P, Gallais L, Hebert D, Mainfray C, et al. Infrared thermometry and interferential microscopy for analysis of crater formation at the surface of fused silica under CO_2 laser irradiation. J Appl Phys 2012;111:063106.
[27] Jiang Y, He S, Liao W, Yao C, Wang H, Wang B, et al. Theoretical and experimental investigations of localized CO_2 laser-fused silica interactions and thermo-mechanical properties of mitigated sites. J Non-Cryst Solids 2019;515:1–10.
[28] Nowak KM, Baker HJ, Hall DR. Analytical model for CO_2 laser ablation of fused quartz. Appl Opt 2015;54:8653–63.
[29] Feit MD, Rubenchik AM. Mechanisms of CO_2 laser mitigation of laser damage growth in fused silica. Laser-Induced Damage in Optical Materials: 2002 and 7th International Workshop on Laser Beam and Optics Characterization, International Society for Optics and Photonics. 2002. p. 91–103.
[30] Doualle T, Gallais L, Cormont P, Hébert D, Combis P, Rullier J-L. Thermo-mechanical simulations of CO_2 laser–fused silica interactions. J Appl Phys 2016;119:113106.
[31] Doualle T, Hébert D, Combis P, Hecquet C, Gallais L, Rullier J-L. Comparison between fused silica of type II and III after surface heating with a CO_2 laser. Appl Phys A 2016;122:90.
[32] He T, Wei C, Jiang Z, Yu Z, Cao Z, Shao JJCOL. Numerical model and experimental demonstration of high precision ablation of pulse CO_2 laser. Chinese Optics Letters 2018;16:041401.
[33] Sharma S, Mandal V, Ramakrishna S, Ramkumar J. Numerical simulation of melt hydrodynamics induced hole blockage in Quasi-CW fiber laser micro-drilling of TiAl6V4. J Mater Process Technol 2018;262:131–48.
[34] Combis P, Cormont P, Gallais L, Hebert D, Robin L, Rullier J-L. Evaluation of the fused silica thermal conductivity by comparing infrared thermometry measurements with two-dimensional simulations. Appl Phys Lett 2012;101:211908.
[35] Doremus RH. Viscosity of silica. J Appl Phys 2002;92:7619–29.
[36] Zhao L, Cheng J, Chen M, Yuan X, Liao W, Wang H, et al. Toward little heat-affected area of fused silica materials using short pulse and high power CO_2 laser. Results Phys 2019;12:1363–71.
[37] Vignes RM, Soules TF, Stolken JS, Settgast RR, Elhadj S, Matthews MJ. Thermomechanical modeling of laser-induced structural relaxation and deformation of glass: volume changes in fused silica at high temperatures. J Am Ceram Soc 2013;96:137–45.